Ultrasonics Sonochemistry 90 (2022) 106203

Contents lists available at ScienceDirect

Ultrasonics Sonochemistry

journal homepage: www.elsevier.com/locate/ultson

Microstructural evolution and mechanical properties of TiB_2/2195 composites fabricated by ultrasonic-assisted in-situ casting

Ziming Xie [a,b], Ripeng Jiang [a,b,*], Xiaoqian Li [a,b,c], Lihua Zhang [a,b,c], Anqing Li [a,b], Zhuoli He [a,b]

[a] Light Alloy Research Institute, Central South University, Changsha 410083, China
[b] State Key Laboratory of High Performance Complex Manufacturing, Changsha 410083, China
[c] College of Mechanical and Electrical Engineering, Central South University, Changsha 410083, China

ARTICLE INFO

Keywords:
Ultrasonic-assisted casting
Al-Li alloy
Composite
In-situ TiB_2

ABSTRACT

The distribution and size of particles in particle-reinforced aluminum matrix composites are crucial to the mechanical properties of the composites. In this paper, 2 wt.% TiB_2/2195 composites were prepared by ultrasonic-assisted in-situ casting technology, and the samples' phase composition, microstructure, and mechanical properties were tested. The results showed that: compared with the remelted matrix, the stomatal defects in the composites disappeared, and the grains were refined, but the second phase structure and TiB_2 particles agglomerated significantly when no ultrasonic treatment (UT) was applied. The UT made the grains further refined, the area fraction of the coarse second phase network decreased, the concentrations of Ti and Cu elements in the grains increased, and more TiB_2 particles entered the grains. At the same time, the formation of TiB_2 particles and UT increased the dislocation density in the composites and promoted the precipitation of the T1 phase. With UT for 180 s, the TiB_2 particles were evenly distributed, and the size was the smallest. The tensile strength, yield strength, and elongation were increased by 115.4 %, 49.8 %, and 342.9 %, respectively, compared to the remelted matrix, and by 30.9 %, 21.8 %, and 67.2 %, respectively, compared to the composite without UT. The mechanism of the synergistic effect of UT and TiB_2 to enhance the mechanical properties of composites was also discussed.

1. Introduction

Aluminum matrix composites (AMCs) have an excellent specific strength, specific stiffness, high-temperature resistance, and corrosion resistance, so they have a wide range of application prospects in the fields including automobile, chemical industry, biomedicine, and aerospace [1–4]. Particle-reinforced aluminum matrix composites (PRAMCs) is a composite material that combines the excellent toughness and plasticity of the metal with the high hardness and high modulus of the reinforcing particles by combining the reinforcing phase of the ceramic particles with the aluminum alloy matrix. Two methods can obtain the particles in PRAMCs: external addition and in-situ synthesis. Compared with the external addition method, the in-situ PRAMCs have the advantages of a clean interface and good interface bonding [5–7], but the reinforced particles prepared by the in-situ method are prone to agglomeration. Wang et al. [8] successfully synthesized in situ TiB_2/A356 composites through the salt-metal reaction route, and TiB_2 clusters were randomly distributed on the grain boundaries. Zhang et al. [9] prepared in-situ (TiB_2 + ZrB_2)/AlSi9Cu3 composites using the Al-K_2TiF_6-K_2ZrF_6-KBF_4 system as raw materials. They found that the particles agglomerated into many "reinforcing groups" distributed along the matrix grain boundaries, and the number of particle clusters increased with the increased mass fraction of reactant. The agglomerated particles will form voids or porosities between adjacent particles, resulting in an uncompacted microstructure [10], and may also become crack initiation sites [11].

In response to this problem, researchers have tried various methods, among which ultrasonic-assisted casting has proved effective in agglomerating dispersed particles and refining solidified structures. Huang et al. [12] prepared TiB_2/2A14 in situ composites with a volume fraction of 3 % by combining mixed salt reaction and high-energy ultrasound. The results showed that ultrasonic vibration could effectively improve the distribution of particles. High-pressure shock waves scattered the large-volume agglomerated particles into small-volume

* Corresponding author at: Light Alloy Research Institute, Central South University, Changsha 410083, China.
E-mail addresses: xieziming@csu.edu.cn (Z. Xie), jiangrp@csu.edu.cn (R. Jiang), meel@csu.edu.cn (X. Li), zhanglihua@csu.edu.cn (L. Zhang), laq0823@csu.edu.cn (A. Li), hzl333@csu.edu.cn (Z. He).

https://doi.org/10.1016/j.ultsonch.2022.106203
Received 23 July 2022; Received in revised form 8 October 2022; Accepted 11 October 2022
Available online 12 October 2022

aggregated or dispersed particles and diffused them uniformly into the melt by acoustic streaming. After ultrasonic vibration treatment for 120 s, the agglomerated particles were basically eliminated. Liu et al. [13] applied ultrasound-assisted solidification (UAS) to the fabrication of nano-sized TiB_{2p}/Al-4.5Cu composites, and the results showed that UAS could significantly refine the microstructure of the Al-4.5Cu matrix and induce more TiB_2 particles distributed in α-Al grains. Yang et al. [14] used the A356-K_2TiF_6 system as raw material to prepare 5 wt.% Al_3Ti/A356 in-situ composites with high strength and good plasticity by ultrasonic-assisted in-situ casting at 800 °C. The particles were uniformly distributed in the matrix, most of which were located inside the α-Al crystals.

In the current studies on PRAMCs, relatively few have used Al-Li alloys as matrix materials. Lithium (Li) is the lightest metal element in nature. Compared with commonly used 2XXX and 7XXX alloys, Al-Li alloys have higher specific strength and specific stiffness [15]. The AMCs with higher specific strength and specific stiffness can be obtained by selecting them as the matrix of the composite. In addition, according to the Orowan strengthening theory, the existing research also proves that only the dispersed and fine ceramic particles entering the α-Al grains will effectively strengthen the matrix. However, there are few studies on quantitatively analyzing the distribution of reinforcement particles in the grains caused by ultrasonic-assisted casting and their effects on mechanical properties.

In this paper, TiB_2 particle-reinforced aluminum matrix composites were prepared by in-situ synthesis using 2195 Al-Li alloy as the matrix. The mass fraction of TiB_2 particles was preset to 2 % to ensure the strengthening effect without affecting the material density too much. The effects of UT and in-situ TiB_2 particles on the microstructure and properties of composites were analyzed, and the mechanism of the synergistic effect of ultrasonic and TiB_2 to improve mechanical properties was discussed.

2. Materials and methods

2.1. Materials

The composition of the 2195 Al-Li alloy matrix used in this experiment is shown in Table 1, which was detected by an Inductively Coupled Plasma Atomic Emission Spectrometer (ICP-AES, SPECTRO BLUE, Germany). The raw materials used for the in-situ reaction to generate TiB_2 were K_2TiF_6, KBF_4, and Na_3AlF_6 (analytical grade) provided by Tianjin Kemiou Chemical Reagent Co., Ltd.

2.2. Composite preparation

The experimental system is shown in Fig. 1, which mainly includes a resistance furnace, a graphite silicon carbide crucible, an inert gas protection device, an ultrasonic vibration system, and a thermometer. The ultrasonic vibration system comprises an ultrasonic generator with a maximum output power of 2 kW, an air-cooled piezoelectric transducer (~20 kHz), an ultrasonic amplitude transformer, and a cylindrical Ti alloy ultrasonic sonotrode with a tip diameter of 50 mm [16].

First, about 650 g of 2195 Al-Li alloy matrix was weighed, and K_2TiF_6 and KBF_4 powders were taken, respectively, according to the formation amount of 2 wt.% TiB_2. A small amount of Na_3AlF_6 powder was added to the mixed salt powder to promote the reaction. Then, the mixed salt powder was ball-milled for 1 h with a ball-to-powder ratio of 2:1 to make it evenly mixed and then pressed into a round block with a diameter of 50 mm, which was then dried in a drying oven at 200 °C for 2 h.

Table 1
The main components of 2195 Al-Li alloy matrix (wt.%).

Cu	Li	Mg	Ag	Zr	Al
3.99	1.19	0.69	0.37	0.12	Bal.

Meanwhile, the alloy was placed in a silicon carbide graphite crucible with a bottom inner diameter of 70 mm, a top inner diameter of 100 mm, and an internal height of 130 mm, and heated to 780 °C in an argon-filled resistance furnace.

When the matrix was melted entirely, the mixed salt wrapped in aluminum foil was pressed into the melt with a bell jar, and the melt was stirred at a speed of 200 r/min for 1 min by a high-purity graphite impeller stirrer driven by an electric mixer. Ten minutes later, the scum on the melt surface was removed, and the melt temperature was lowered to 720 °C. Then put the preheated ultrasonic sonotrode into the melt, and let the tip surface of the ultrasonic sonotrode be about 20 mm away from the melt surface. Then turn on the ultrasonic power, set the frequency to 20 kHz ± 100 Hz, and set the output power to 400 ± 10 W according to the volume of the melt to ensure that the ultrasonic vibration system works in a stable state. The transducer converts electrical energy into ultrasonic waves containing longitudinal and transverse waves, which propagate along the axial and radial directions of the ultrasonic sonotrode, respectively, causing the tip surface of the ultrasonic sonotrode to generate vibrations with an amplitude of 11.3–12.6 μm [17], which are finally transmitted to the melt. The UT time was set to 0 s, 60 s, 120 s, 180 s, and 240 s, respectively. The alloy melt was poured into a high-purity graphite mold with an inner diameter of ∅55 × 110 mm after UT and air-cooled to room temperature to obtain a composite round ingot. In addition, the remelted 2195 matrix was prepared as a control sample under the same experimental parameters but without UT (i.e., UT 0 s). The ultrasonic sonotrode was also put into the melt in the experiments without UT, but the ultrasonic power was not turned on to ensure consistent experimental conditions.

2.3. Microstructural analysis and tensile properties test

As shown in Fig. 2 [10,18], samples were taken from the ingots to characterize the microstructure and mechanical properties of the material. The phase composition of the samples was determined using an X-ray diffractometer (XRD, Bruker D8 advance, Germany). The microstructure of samples was observed with a scanning electron microscope (SEM, TESCAN MIRA3, Czech Republic) equipped with an energy dispersive spectrometer (EDS), and the inner regions of 3 different grains were randomly selected in each sample for EDS element mapping analysis to measure the concentrations of elements such as Ti and Cu inside the grains. Image analysis software (Image-Pro Plus, IPP) was used to quantitatively analyze the area fraction of the second phase and the particle size of TiB_2 particles. The metallographic structure of the samples etched with Keller's reagent (95 % H_2O, 2.5 % HNO_3, 1.5 % HCl, and 1 % HF) was observed by optical microscopy (OM, OLYMPUS DSX500, Japan). The SEM (Thermofisher Helios 5CX, USA) equipped with an electron backscatter diffractometer (EBSD, EDAX HIKARI Super, USA) was used to perform EBSD scanning of the samples, and the EBSD data were post-processed on TSL-OIM software to obtain the grain size and TiB_2 particle distribution. The line interception method calculated the grain size (ASTM 112–10) [19]. The samples tested above were mechanically ground and polished according to standard metallographic techniques before testing, and the EBSD samples were additionally polished with a 0.5 μm particle size SiO_2 polishing solution for 3 h. It should be noted that the XRD data, SEM images, and OM images were all from the samples at the core of the ingot, and the top and bottom samples were only used to quantitatively analyze the concentrations of Cu and Ti elements inside the grains. The ground tensile samples were subjected to a room temperature (25 °C) tensile test on an electronic universal testing machine (CMT5105GL, China) at a tensile speed of 2 mm/min to obtain ultimate tensile strength (UTS), yield strength (YS), and elongation of each group of samples, and elastic modulus of the matrix. All tensile tests were repeated three times to ensure the reliability of the results. The SEM (TESCAN MIRA3, Czech Republic) was used to observe the fracture surface.

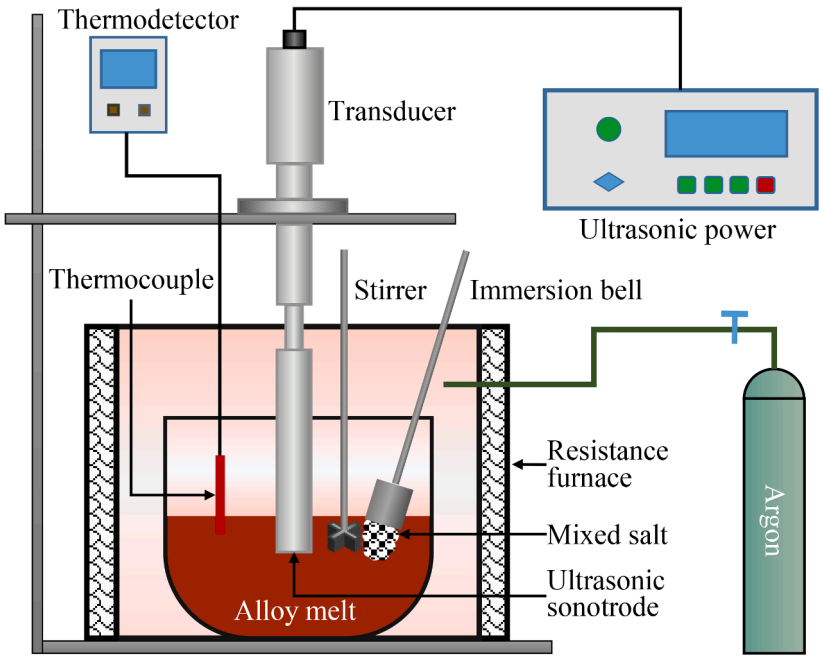

Fig. 1. Schematic diagram of the experimental system.

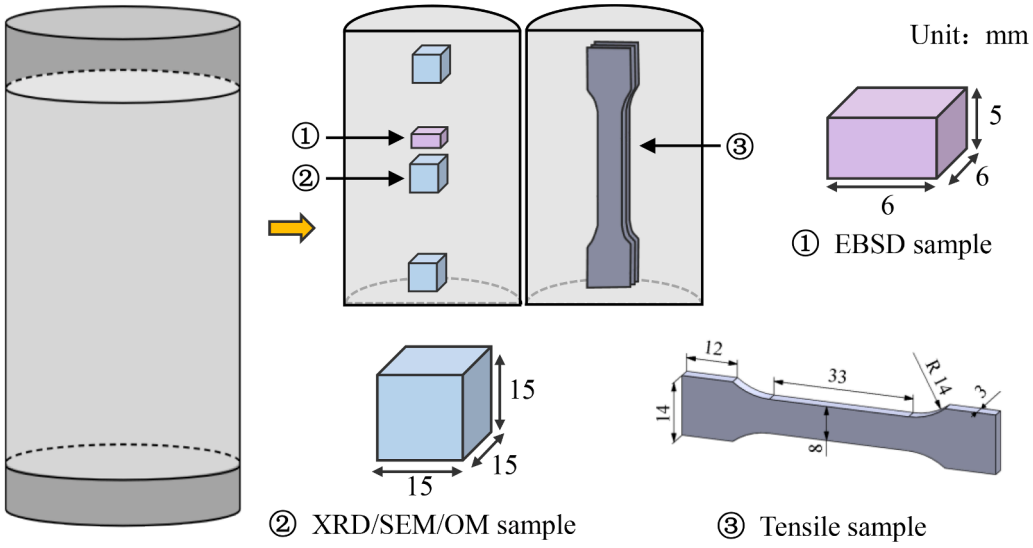

Fig. 2. Schematic diagram of sampling.

3. Results

3.1. Phase analysis

The XRD patterns of the samples are shown in Fig. 3a, and the diffraction peaks of α-Al, θ'- Al_2Cu, δ-AlLi, and T2-Al_6CuLi_3 phases appear simultaneously in all samples. However, T1-Al_2CuLi phase diffraction peaks are pronounced in composites but not in the matrix, and UT has improved the intensity of diffraction peaks. In addition, TiB_2 diffraction peaks also appeared in the composite material, indicating that the in-situ reaction generated TiB_2 particles.

3.2. Microstructural evolution

3.2.1. EBSD microstructures

The EBSD analysis results of each sample are shown in Fig. 4, and the black spots in the figures are TiB_2 particles. The grains in the remelted matrix are coarse, and the grain size is discretely distributed between 75 and 550 μm. After the in-situ reaction generated the TiB_2 particles, the grain size was significantly reduced, from 288 μm of the matrix to 159 μm, but the TiB_2 particles agglomerated more seriously at the grain boundaries. After applying UT, the grain size was further reduced, and the TiB_2 agglomeration phenomenon also began to improve. When the UT time was 180 s, the grains were mostly equiaxed, the size was mainly distributed around 70 μm, and about 95 % were smaller than 120 μm. The average grain size was 72 μm, with refinement efficiencies of 75.0 % and 54.7 % compared to the remelted matrix and the composite without UT, respectively. In addition, the large-scale agglomeration at grain boundaries was significantly reduced, and more TiB_2 particles were dispersed inside the grains. When the UT time continued to increase to 240 s, the TiB_2 agglomerates started agglomerating at the grain boundaries again, and the grain size increased to 92 μm simultaneously.

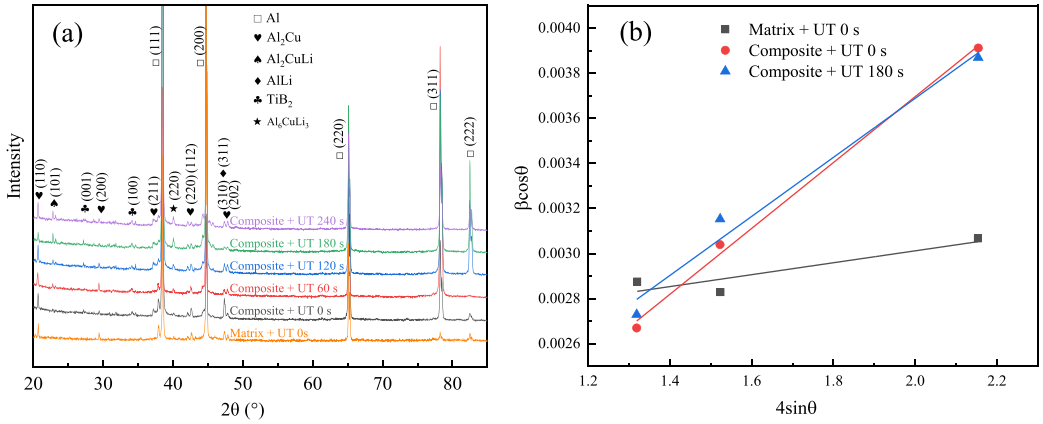

Fig. 3. (a) XRD pattern of remelted matrix and composites. (b) Fitting curve based on XRD data for calculating dislocation density.

The grain size distribution and average grain size are shown in Fig. 5.

3.2.2. SEM microstructures

Fig. 6 shows the microstructure of the samples, including SEM images and OM images, where each inset is the OM image of the corresponding sample. In the remelted 2195 matrix (Fig. 6a), the white second phase has a smooth structure and clear outline and is continuously distributed along the α-Al grain boundary in a network [20]. The agglomeration at the grain boundary connection is accentuated, and a small amount of spherical second phase particles are dispersed in the α-Al grains. In addition, porosities of different sizes can be observed in the OM image, some exceeding 400 μm, and the micropore is also found in the SEM image. With the formation of TiB_2 particles in the in situ reaction, the second phase profile becomes relatively blurred and flocculent, and there are no apparent porosities (Figs. 6b-f). In the solidified structure without UT, the agglomeration phenomenon is more serious, and the maximum diameter of the agglomerate exceeds 100 μm, as shown in Fig. 6b. The boxed area in the figure is analyzed by EDS element mapping, and the result is shown in Fig. 6g, indicating that the second phase structure of the agglomeration is mainly TiB_2 particles and Cu-containing phases such as Al_2Cu, and Al_2CuLi.

With the application of UT, the large agglomerates were broken up, and the maximum diameter of the agglomerates began to decrease. When UT was applied for 60 s, the maximum diameter of the agglomerates decreased to about 70 μm. The increase in UT time further reduced the maximum diameter of aggregates, and when the UT time was 120 s, its value was about 40 μm. When the UT time continued to increase to 180 s, its value decreased to about 30 μm, and more fine particles were dispersed into the Al matrix. Fig. 6h is a partially enlarged view of the inner grain of the composite material (the area selected in Fig. 6e) with UT for 180 s. The EDS elemental mapping analysis shows that there are many TiB_2 particles dispersed in the α-Al matrix (as indicated by the arrow). However, when the UT time continued to increase to 240 s, the maximum diameter of the aggregates increased to about 50 μm, which was consistent with the changing trend of the EBSD analysis results. The change in grain size shown in the OM images is also compatible with the EBSD results.

Fig. 7a shows each sample's area fraction of the second phase. In the remelted matrix, the area fraction of the entire second phase structure is 4.28 %, and the coarse second phase network (with an area greater than 20 μm^2) [21] is 4.14 %, while in the composites without UT, their values increased to 5.23 % and 4.50 %, respectively, but the ratio of the coarse second phase network to the entire second phase structure decreased from 96.70 % to 86.10 %. After adding UT, all the values began to decline, and when the UT time was 180 s, they were 4.12 %, 3.06 %, and 74.37 %, respectively. Fig. 7b shows the number density (number per mm^2) of precipitated particles (with an area less than 20 μm^2) [18] inside the grains. In the composite material without UT, the value is 1830.0, which is significantly higher than that of the remelted matrix of 771.5, the UT improved it further, and the number density was the largest at 2912.4 when UT was performed for 180 s.

Fig. 7c shows the concentrations of Ti and Cu elements in the α-Al grains of the remelted matrix and composites. In the remelted matrix, the Cu concentration in the grains is 1.62 wt.%, and the Ti concentration is close to 0. After the in-situ reaction generated TiB_2 particles, the Ti concentration increased to 0.10 wt.%, while the Cu concentration decreased to 1.09 wt.%. After applying UT, the concentrations of Ti and Cu elements in the grains began to increase. When the UT time was 180 s, the concentrations of Ti and Cu increased to 0.20 wt.% and 2.24 wt.%, respectively, which were 100.0 % and 105.5 % higher than without UT.

To further study the morphology of TiB_2 particles and their distribution in the composites, the agglomerates were observed with higher magnification, and the results are shown in Fig. 8. When UT was not applied (Fig. 8a), most TiB_2 particles interlaced with the Cu-containing phase to form cloud-like or ice-like agglomerates. The identifiable TiB_2 particles were mainly polygonal with a maximum diameter of more than 2 μm. When UT was applied for 60 s (Fig. 8b), the agglomeration phenomenon was significantly improved, and TiB_2 particles with regular shape, clear outline, the polygonal or nearly circular form could be observed, and the diameter was mainly about 0.5 μm. However, the TiB_2 particles were still relatively dense. When the UT time increased to 120 s (Fig. 8c), many TiB_2 particles began to disperse, and the particle size also became smaller. When the UT time increased to 180 s (Fig. 8d), the overlapping and aggregation of TiB_2 particles were further improved, and many particles were dispersed inside the grains. Most particles were less than 0.3 μm, and many were about 100 nm or even less than 100 nm. EDS analysis was performed on the white particle indicated by the arrow in Fig. 8d, and the results are shown in Fig. 8f, and it was determined that they were TiB_2 particles. It indicates that UT can also change the morphology and size of TiB_2 particles while preventing agglomeration.

3.3. Mechanical properties

The room temperature tensile test results of the samples are shown in Fig. 9. It can be seen from Fig. 9b that the average values of the UTS, YS, and elongation of the remelted matrix are 90.7 MPa, 57.8 MPa, and 1.72 %, respectively. For the composite material without UT, its values increased to 149.2 MPa, 71.0 MPa, and 4.56 %, respectively. After UT was applied to the composite, the strength and elongation were further improved. When the UT time was 180 s, the UTS, YS, and elongation increased to 195.3 MPa, 86.5 MPa, and 7.62 %, respectively. The improvements were 115.4 %, 49.8 %, and 342.9 %, respectively, compared with the remelted matrix, and 30.9 %, 21.8 %, and 67.2 %, respectively, compared with the composite material without UT. However, when the

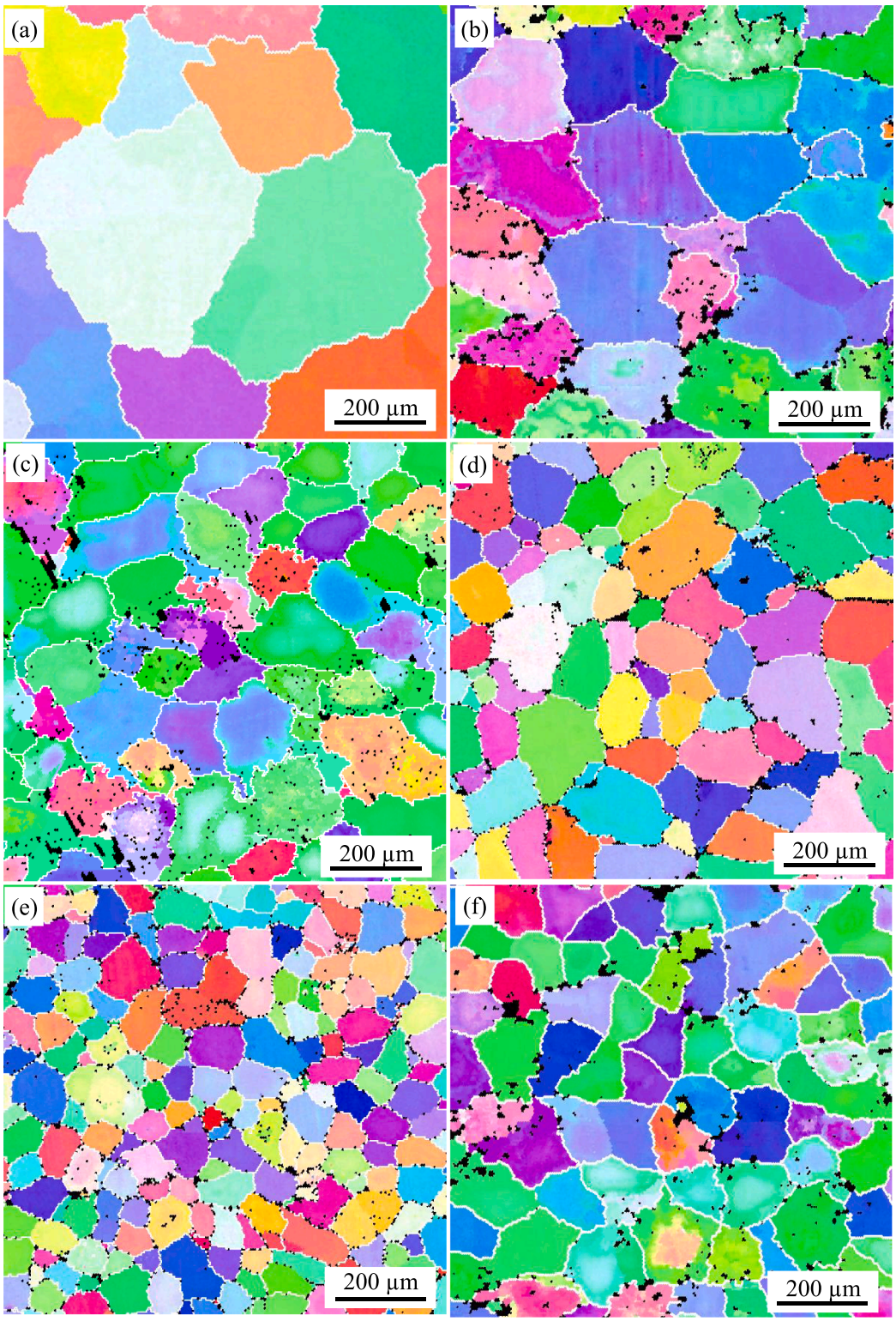

Fig. 4. EBSD orientation map of remelted matrix (a) and composites: (b) without UT, (c) UT for 60 s, (d) UT for 120 s, (e) UT for 180 s, (f) UT for 240 s.

UT time continued to increase to 240 s, the composite's UTS, YS, and elongation began to decrease.

The fracture surface of the remelted matrix shown in Fig. 10a has apparent cracks, pores, and a large number of coarse grape-like dendritic structures [22], which are the main reasons for its poor mechanical properties. On the fracture surface of the composite without UT shown in Fig. 10b, the dendritic structure disappeared, mainly including cleavage planes, cleavage steps, and coarse tear ridges, and there were a few dimples around the tear ridges. Upon further observation, many small cracks are on the fracture surface, as shown in Fig. 10g. The EDS mapping analysis shows that the periphery of the cracks is agglomerates composed of TiB_2 and Cu-containing phases. The matrix around these agglomerates has minimal slip space, and its local deformation is more significant than the near-planar interface [23], which can be a source of cracks. Figs. 10c-f are the fracture morphologies of the ultrasonically treated composites, all showing a mixed fracture mechanism. The coarse

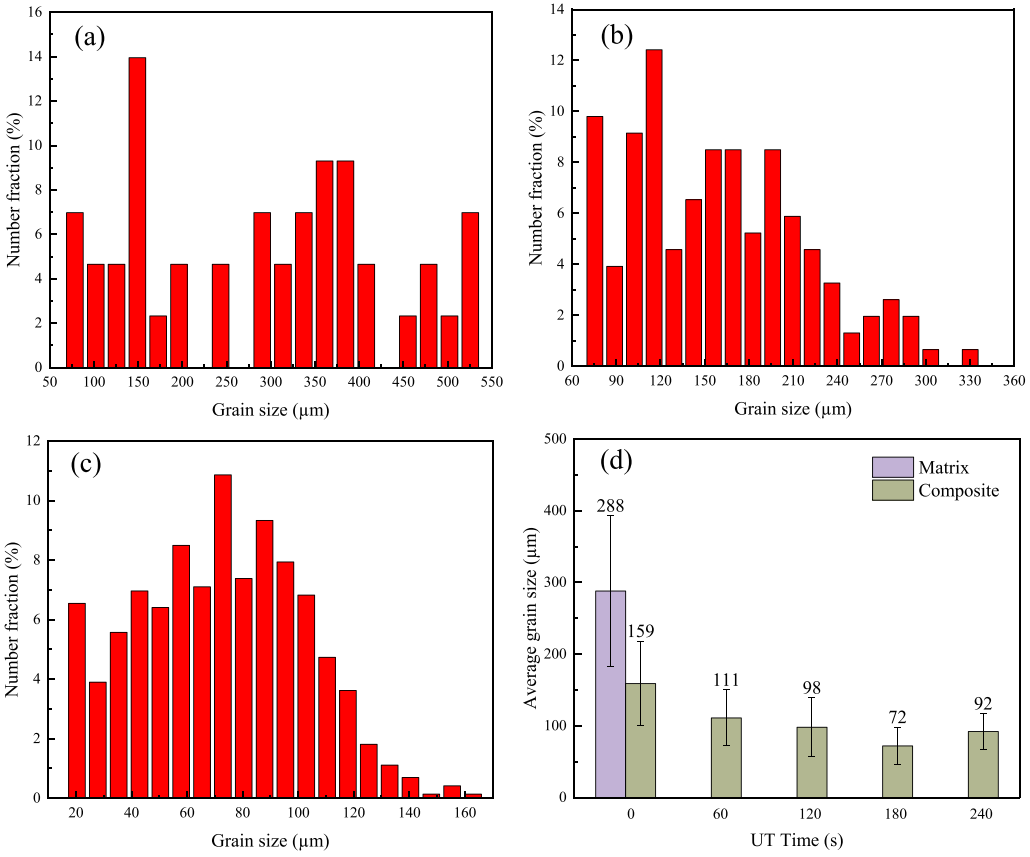

Fig. 5. Grain size distribution of remelted matrix (a) and composites: (b) without UT, (c) UT for 180 s. (d) The average grain size of the remelted matrix and composites with different UT times.

tear ridges and cleavage planes on the fracture surface decrease, and the cleavage planes and dimples in small areas increase. When the UT time was 180 s, many small tearing ridges and dimples were distributed on the fracture surface. Dispersed and well-defined nano or submicron particles were found at the bottom of the dimples, as shown in Fig. 10*h*, which were confirmed to be TiB_2 particles by EDS analysis (as shown in the inset). It shows that some TiB_2 particles enter the matrix and combine well with the matrix.

4. Discussion

4.1. The effect of TiB_2 particles on the evolution of microstructures

TiB_2 particles have a good crystal orientation relationship with Al, and the lattice mismatch is less than 5 % [24], which can act as the nucleus for Al solidification and inhibit grain growth [25]. The relationship between the number of nucleation sites and grain size can be described as [18,26]:

$$D_{gs} = \frac{D\Delta T_n}{vQ} + \frac{1}{\sqrt[3]{f\rho}} \tag{1}$$

where D_{gs} is the grain size, D is the diffusion coefficient of solute atoms, ΔT_n is the additional undercooling required for nucleation, v is the growth rate of α-Al grains, Q is the confinement factor of the grains, f is The percentage of heterogeneous particles participating in the nucleation process, and ρ is the number density of heterogeneous particles in the aluminum melt. This formula shows that when other conditions remain unchanged, the increase in the number of heterogeneous nucleation will promote grain refinement. The TiB_2 particles generated in the in situ reaction provide many heterogeneous nucleation sites for the melt, which leads to grain refinement.

However, not all TiB_2 particles will become α-Al nuclei since there is a critical velocity at the solidification front below which particles will be pushed to the advancing front and agglomerate at the grain boundaries [27]. Although the TiB_2 particles at the grain boundaries can play the role of Zener pinning particles, which can prevent the migration of grain boundaries and further inhibit the growth of α-Al grains [24], the TiB_2 clusters will hinder the flow of solute atoms such as Cu. In addition, the Al_2Cu phase and TiB_2 particles have good wettability. During the solidification process, the Al_2Cu phase and TiB_2 clusters will be entangled, forming a continuous and coarse second phase network at the grain boundary. Therefore, after the formation of TiB_2 particles, the content of Cu element in the grains decreases, and the area fraction of the second phase increases.

In addition, TiB_2 particles have different coefficient of thermal expansion (CTE) values from the matrix. During the composite material's solidification process, many dislocations will be generated at the interface between the matrix and the reinforcing particles due to the thermal mismatch between the matrix and the reinforcing particles. The dislocation density can be calculated by the following formula [28,29].

$$\rho = \frac{2\sqrt{3}e}{db} \tag{2}$$

where b is the Burger vector (about 0.286 nm for Al [30]), d is the crystallite size, and e is the microstrain. d and e are generally estimated by the Williamson-Hall method combined with XRD data using the following equation [28,29].

$$\beta\cos\theta = \frac{\lambda}{d} + 4e\sin\theta \tag{3}$$

where θ is the Bragg angle and λ is the wavelength of the Cu kα radiation (0.154 nm).

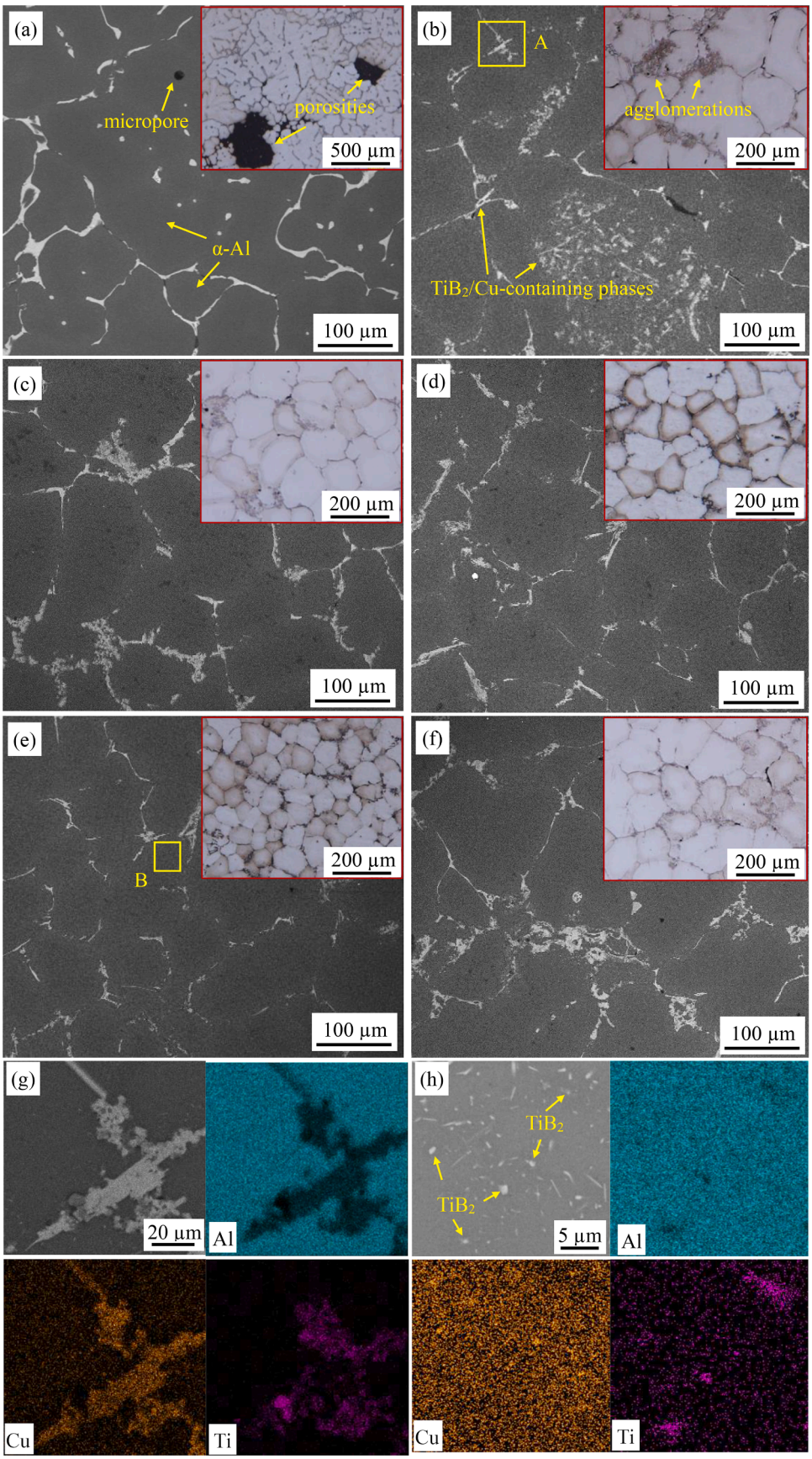

Fig. 6. SEM and OM images (inset) of remelted matrix (a) and composites: (b) without UT, (c) UT for 60 s, (d) UT for 120 s, (e) UT for 180 s, (f) UT for 240 s. (g) and (h) are the magnified SEM images and EDS elemental mapping analysis of the boxed areas A and B in (b) and (e), respectively.

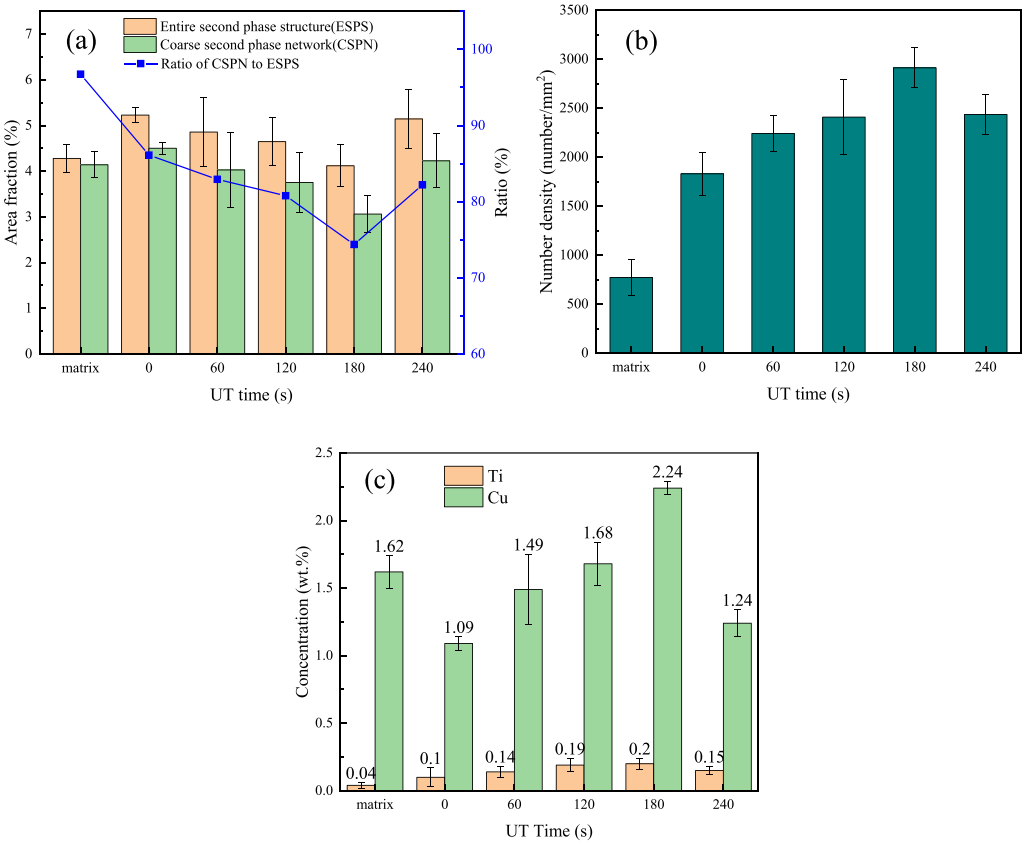

Fig. 7. (a) The area fraction of the second phase. (b) The number density of precipitated particles and (c) concentrations of Ti and Cu inside the grains.

Eq. (3) shows that the crystallite size d and the microstrain e can be calculated from the intercept and slope of the straight line fitted by the $4sin\theta$ and $\beta cos\theta$ values shown in Fig. 3b. Then, the dislocation densities of the remelted matrix, the composite without UT and with UT for 180 s can be calculated by Eq. (2) to be 5.157×10^{13}, 8.159×10^{13}, and 1.102×10^{14} m^{-2}, respectively. It shows that the dislocation densities in the composites are significantly higher than that in the matrix, and the dislocation density of the composite after UT for 180 s is more than twice that of the matrix.

Existing studies have demonstrated that the T1 phase usually nucleates on dislocations [31,32]. The high density of dislocations in the composite provides additional heterogeneous nucleation sites for the T1 phase. It can notably reduce the critical energy for nucleation, promote the precipitation process of the T1 phase, and significantly increase the number density of the T1 phase [11]. Therefore, the diffraction peak of the T1 phase appears in the composite but is not evident in the matrix. On the one hand, the quantity of the T1 phase in the matrix may be small [27]; On the other hand, it shows that the in-situ generated TiB_2 can promote the precipitation of the T1 phase.

4.2. The effect of UT on the evolution of microstructures

It can be seen from the previous results that UT can not only refine grains but also change the microstructure of the second phase, refine particles and prevent particle agglomeration. It is generally considered that this is the synergistic effect of acoustic streaming and ultrasonic cavitation [21,33–35].

The possible mechanism of UT regulating the microstructure of composites is shown in Fig. 11. When ultrasonic vibration is introduced into the melt, due to the alternation of positive and negative acoustic pressures of ultrasonic waves, numerous tiny cavitation bubbles (bubble clouds) will be generated near the sound source [36]. At the same time, the acoustic pressure gradient formed when the acoustic wave propagates in the melt will cause eddy currents inside the melt to create an acoustic streaming effect, as shown by the curve with arrows in Fig. 11. On the one hand, the acoustic streaming can promote the melt flow, stir the melt, prevent the formation of coarse dendrites and particle clusters, and promote the diffusion of solute elements. On the other hand, acoustic streaming pushes the cavitation bubbles to move, and the cavitation bubbles merge or devour each other and grow continuously during the movement. In addition, the periodic variation of acoustic pressure also promotes the spontaneous growth of cavitation bubbles. Cavitation bubbles will collapse when their internal pressure reaches a specific value, and at the instant of collapse, a high-energy shock wave exceeding 1000 MPa and a micro-jet with a speed of about 100 m/s will be generated [37,38]. Shock waves and microjets will break up the growing dendrites and TiB_2 particle agglomerates and disperse the solute atoms that have aggregated at the grain boundaries. The detached branches will be transported several times by the recirculating acoustic streaming to the cavitation zone, where they will experience further fragmentation by imploding bubbles, producing small dendrite fragments that act as nuclei of the intermetallic phase in the subsequent solidification [35]. Dendrites fragmentation to non-dendrites will significantly reduce eutectic structure at grain boundaries during solidification, thereby refining the second phase structure [38]. At the same time, the shock wave and microjet will also wash the surface of the particles, strip the impurities on their surface, improve their wettability with the melt and involve them in the solidification process [39], further increasing heterogeneous nucleation.

With the increase of UT time, the number of dendrites and agglomerates that were broken and dispersed gradually increased, the number density of TiB_2 particles increased, the distribution of TiB_2 particles and solute atoms became more uniform, and the number of nucleated cores progressively increased so that the grains were steadily refined. More

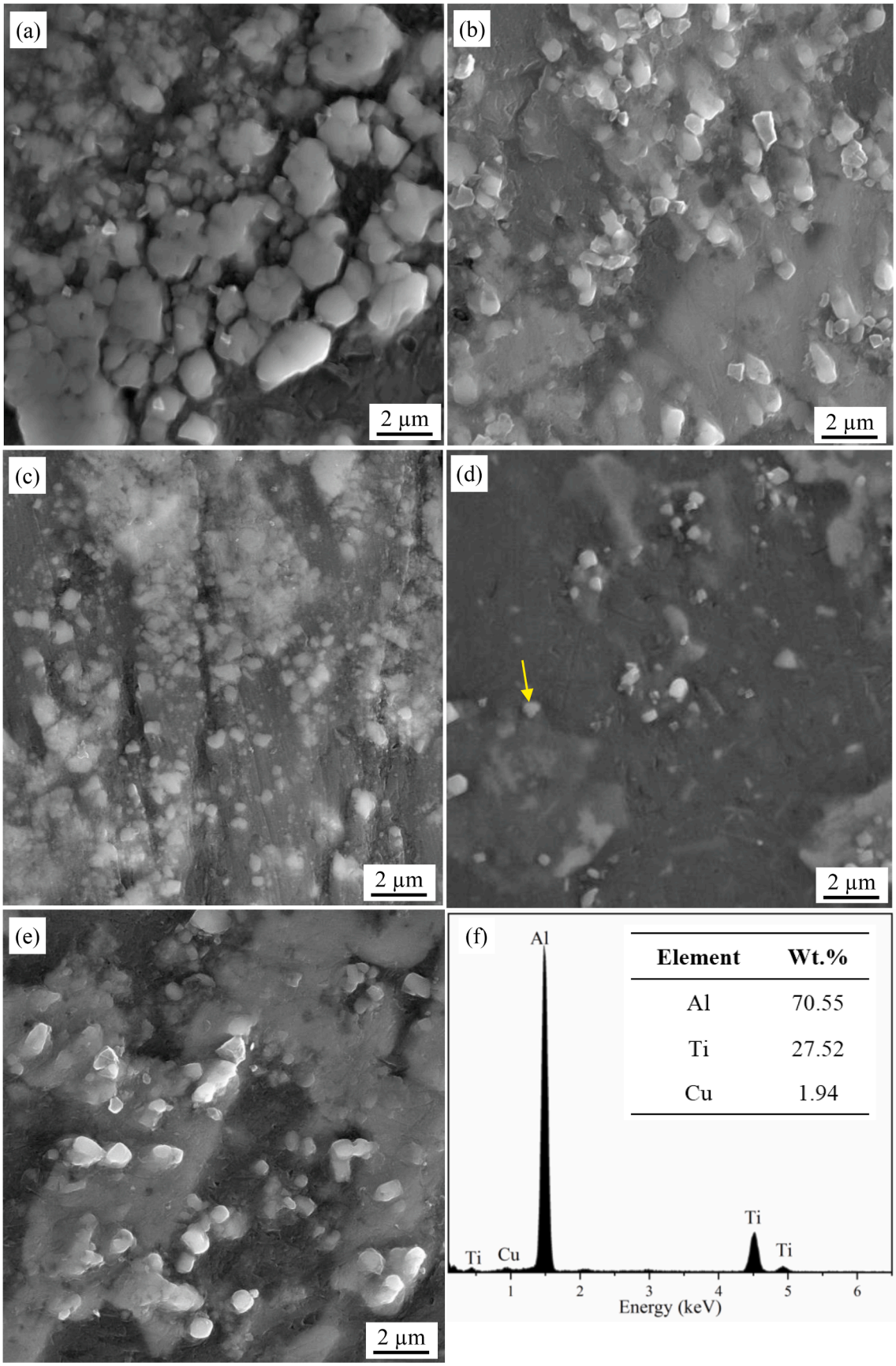

Fig. 8. Morphology of TiB_2 particles in composites with different UT times: (a) 0 s, (b) 60 s, (c) 120 s, (d) 180 s, (e) 240 s. (f) EDS analysis of the particle indicated by the arrows in (d).

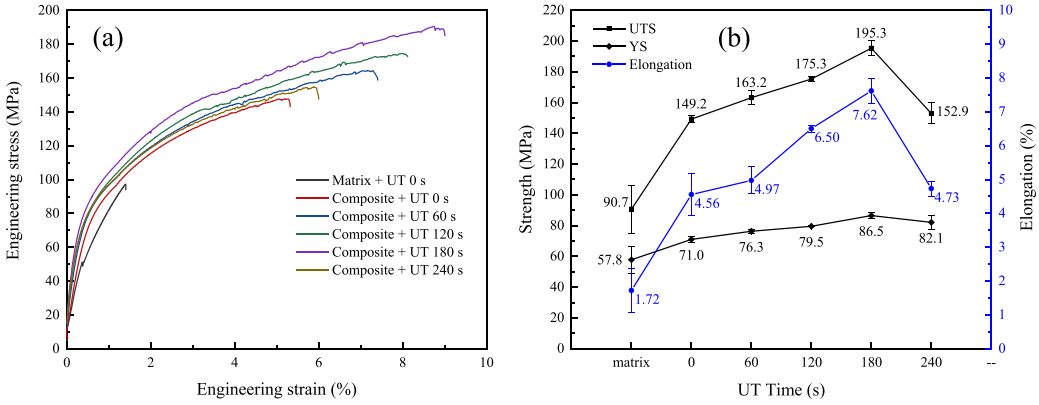

Fig. 9. Mechanical properties: (a) stress–strain curve, and (b) average value of UTS, YS, and elongation.

tiny TiB_2 particles and solute elements enter the interior of the α-Al grains. At the same time, the refinement and equiaxed distribution of grains will increase the grain boundary area, which provides more precipitation sites for the precipitation of Cu-containing phases, which is also beneficial in preventing the formation of coarse second-phase networks [21,40]. In addition, the dispersed second phase can also provide heterogeneous nucleation for the Al melt. That is, the refinement of grains and the refinement of the second phase structure will promote each other. Therefore, with the increase of UT time, the area fraction of the coarse second phase network and its proportion in the entire second phase structure gradually decreased. In contrast, the number density of precipitated particles inside the grains increased, and the mass fraction of solute elements inside the grains increased accordingly. Moreover, the increased number density and uniform distribution of TiB_2 particles benefit the growth and uniform distribution of dislocations. Therefore, the T1 phase diffraction peak intensity rose in the composites with UT.

However, the effect of grain refinement and dispersion agglomeration is not entirely positively correlated with the UT time. When the UT exceeds a particular time, the melt and particles near the acoustic source will absorb too much heat, resulting in the energy of the dispersed second phase and TiB_2 particles rising and spontaneous agglomeration. At the same time, the ultrasonic acoustic streaming will force the particles to move to the acoustic pressure node. When the time is too long, the particles will gather at the low acoustic pressure position, thus weakening the effect of UT. In this study, the effect of UT became more significant with the increase of time in the range of 0 to 180 s, and it began to weaken after more than 180 s, so the optimal UT time was 180 s. The variation trend of grain size with UT time is consistent with the findings of Huang et al. [12].

4.3. The mechanism of UT and TiB_2 particles synergistic to improve mechanical properties

4.3.1. Strength

The increase in YS of PRAMCs is usually attributed to the following aspects [11,22,41]: grain refinement ($\sigma_{Refinement}$), Orowan strengthening (σ_{Orowan}), CTE mismatch strengthening (σ_{CTE}), and load-bearing strengthening (σ_{Load}). The mechanical properties of the ultrasonically treated composites are further improved because UT not only refines the grains but also disperses the agglomerated TiB_2 particles and refines the size of the TiB_2 particles, which promotes the above four types of strengthening. The TiB_2 particles shown in Fig. 10*h* were at the bottom of the dimples and did not fall off, indicating that the TiB_2 particles entered the interior of the grains and were well combined with the matrix. When subjected to external loads, these dispersed TiB_2 particles will improve the ability of the matrix to resist deformation, thereby improving the material's mechanical properties. Therefore, the improvement of mechanical properties results from the synergistic effect of UT and TiB_2 particles, and the possible mechanism is shown in Fig. 12. The following formula can calculate the theoretical improvement of YS by various strengthening effects [42]:

$$\Delta\sigma = \Delta\sigma_{Refinement} + \Delta\sigma_{Load} + \left(\left(\Delta\sigma_{Orowan}\right)^2 + \left(\Delta\sigma_{CTE}\right)^2\right)^{1/2} \tag{4}$$

Then the predicted YS ($\sigma_{predicted}$) can be calculated by:

$$\sigma_{predicted} = \Delta\sigma + \sigma_m \tag{5}$$

where σ_m = 57.8 MPa is the YS of the matrix, which can be obtained from Fig. 9b.

The contribution of these strengthening mechanisms to the YS of the composite with UT for 180 s is analyzed below.

Both UT and the formation of TiB_2 particles will reduce the grain size. The Hall-Petch strengthening relationship shows that grain refinement can improve the YS of the material, and the relationship is as follows [43,44]:

$$\Delta\sigma_{Refinement} = k_{HP}\left(\frac{1}{\sqrt{d_c}} - \frac{1}{\sqrt{d_m}}\right) \tag{6}$$

where k_{HP} is the corresponding strengthening coefficient of the material (68 MPa $\mu m^{1/2}$ for Al [45]), $d_c = 72\mu m$ is the grain size of the composite, and d_m = $288\mu m$ is the grain size of the matrix, which can be obtained from Fig. 5, respectively.

The different CTEs between the matrix and reinforcing particles will lead to many dislocations at their interface during the composite's solidification, as discussed in section 4.1. The increase in dislocation density will improve the YS, and the following formula can calculate its value [46,47].

$$\Delta\sigma_{CTE} = \eta G_m b\sqrt{\frac{12\Delta\alpha\Delta T V_p}{b d_p\left(1 - V_p\right)}} \tag{7}$$

where η is the strengthening coefficient (1.25 for Al [48,49]), $\Delta\alpha$ is the difference between the CTEs of the matrix and the reinforced particles, and the CTE values of the Al matrix and TiB_2 particle are 25.2 × 10^{-6}/K [46] and 7.8 × 10^{-6}/K [50], respectively, so $\Delta\alpha = 17.4 \times 10^{-6}$/K; ΔT is the difference between the pouring temperature and the test temperature [51], the pouring temperature is 993 K, and the test temperature is 298 K, so ΔT = 695 K; b is the Burger vector;d_p is the average size of the reinforcing particles, about 200 nm in the composite with UT for 180 s. V_p is the volume fraction of the reinforcing particles, and the mass fraction of 2 % is converted into a volume fraction of 1.2 %. G_m is the shear modulus of the matrix, which can be calculated from the following formula [52]:

$$G_m = \frac{E_m}{2(1+v)} \tag{8}$$

where E_m = 32.21 GPa is the elastic modulus of the matrix,

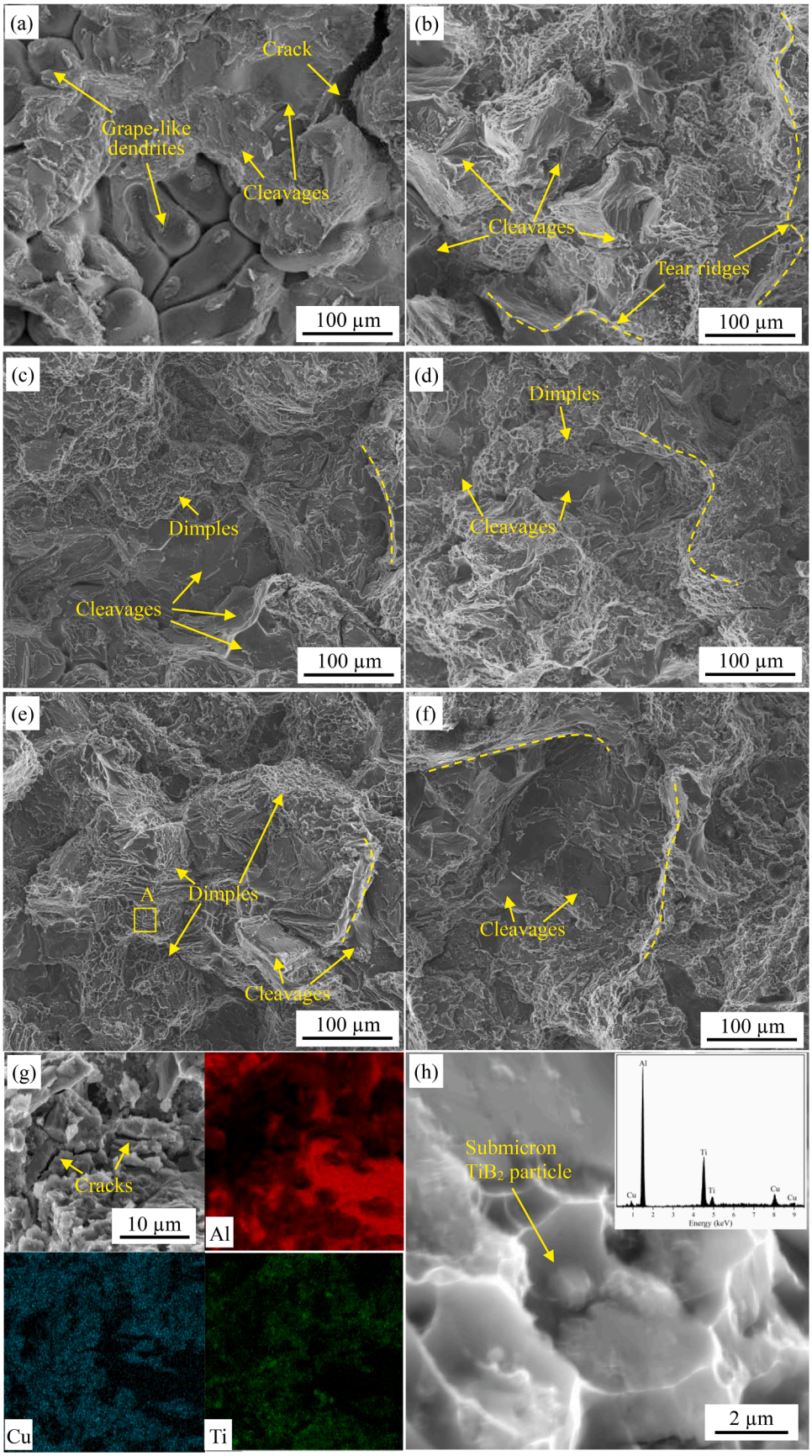

Fig. 10. Tensile fracture surface morphologies of remelted matrix (a) and composites: (b) without UT, (c) UT for 60 s, (d) UT for 120 s, (e) UT for 180 s, (f) UT for 240 s. (g) High magnification SEM image and EDS mapping analysis of composite without UT. (h) Magnified image of the boxed area A in (e).

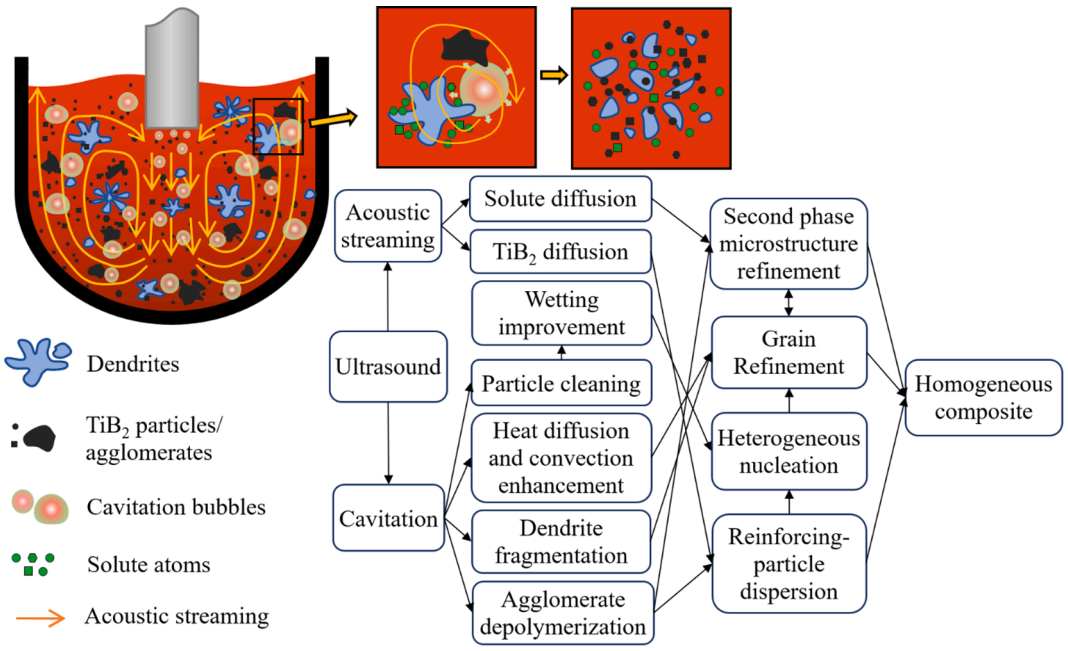

Fig. 11. Schematic diagram of the possible mechanism of ultrasonic-assisted casting to improve the microstructure of composite materials.

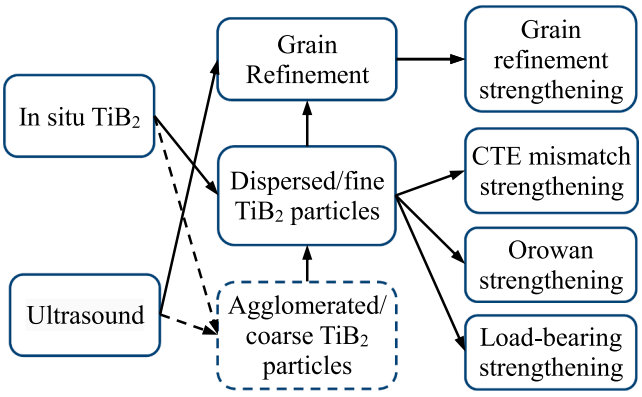

Fig. 12. Schematic diagram of the synergistic strengthening mechanism of UT and TiB_2 particles.

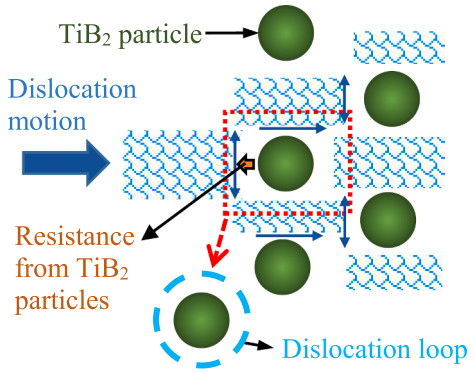

Fig. 13. Schematic diagram of dislocation loop formation.

obtained from tensile tests;$\nu = 0.33$ is the Poisson's ratio of the matrix [50,51]. Therefore, $G_m = 12.1$ GPa can be calculated.

Orowan strengthening comes from the dislocation motion and the interaction between reinforcing particles [52]. When the dislocation interacts with the hard TiB_2 particle, it is difficult for the dislocation to pass through the particle and can only bend around it, thus forming the Orowan bend [49]. When it encounters other hard particles, it will continue to bend, eventually forming a dislocation loop (Orowan loop) around the particle, as shown in Fig. 13. The TiB_2 particles thus form pinning points in the matrix, making it difficult for the surrounding dislocations to move, thereby increasing the strength [53].

In general, the Orowan strengthening mechanism is effective only when the size of the reinforcing particles is less than 1 μm [51]. As shown in Fig. 8d, the size of TiB_2 particles in the composite with UT for 180 s is mostly less than 1 μm, so Orowan strengthening should be considered when predicting YS. In addition, the strengthening effect of the T1 phase can also be described by this mechanism [11]. The contribution of Orowan strengthening to YS can be estimated by the Orowan-Ashby equation [52], as shown below:

$$\Delta\sigma_{Orowan} = \frac{0.13 G_m b}{d_p\left[\left(\frac{1}{2V_p}\right)^{\frac{1}{3}} - 1\right]} ln\frac{d_p}{2b} \tag{9}$$

where G_m is the shear modulus of the matrix, b is the Burger vector, d_p is the average size of the reinforcing particles, and V_p is the volume fraction of the reinforcing particles.

Due to the excellent bonding and clean interface between the matrix and the in situ generated reinforcing particles, the load can be effectively transferred from the soft matrix to the harder TiB_2 particles when subjected to external loads, which is beneficial to the increase of YS [14]. The strength contribution of the load transfer effect can be predicted by the following expression [54,55]:

$$\Delta\sigma_{Load} = 0.5 V_p \sigma_m S \tag{10}$$

where σ_m is the YS of the matrix, and S (close to 1) is the aspect ratio of TiB_2 particles.

The above analysis has given the main parameters in the calculation Eqs. (4)-(10), and the contributions of various strengthening mechanisms to YS in the composite with UT for 180 s calculated based on these parameters are shown in Table 2, and the predicted YS value is close to the measured value ($\sigma_{Measured}$). The CTE mismatch strengthening played a dominant role in these strengthening mechanisms, while other

Table 2
Contributions of different strengthening mechanisms to YS of composite with UT for 180 s (MPa).

$\Delta\sigma_{Refinement}$	$\Delta\sigma_{Orowan}$	$\Delta\sigma_{CTE}$	$\Delta\sigma_{Load}$	$\sigma_{predicted}$	$\sigma_{Measured}$
4.01	5.35	24.03	0.35	86.78	86.50

reinforcement mechanisms produced a minor contribution.

4.3.2. Ductility

The increase in strength and toughness of alloys are contradictory to a certain extent, and the rise in strength often accompanies the decrease in toughness. However, in this study, the composite material has better strength and ductility than the remelted matrix. On the one hand, defects such as porosities in the matrix may be formed by the precipitation of liquid hydrogen dissolved in the Al-Li alloy during solidification [56]. However, no apparent pores were found in the composite material, which may be related to the in-situ reaction and ultrasonic degassing. The in-situ reaction and ultrasonic cavitation will produce a large number of bubbles in the melt, and the hydrogen dissolved in the melt will diffuse into these cavitation bubbles under positive pressure and then form large bubbles and move upward, and finally float to the surface of the melt and escape [57,58], that is, the generation, growth, and flotation of bubbles will constantly remove hydrogen from the melt [59]. On the other hand, grain refinement can disperse the stress in more grains, which is beneficial to the uniformity of deformation [14]. The relationship between strain rate (ε) and grain size can be described by the following equation [51]:

$$\varepsilon = \frac{m}{D_{gs}^{\ 2}}\left(\frac{F}{E}\right) \times 10^{8} \tag{11}$$

Where m is the effective diffusion coefficient, D_{gs} is the grain size, F is the external force, and E is the elastic modulus.

This formula shows that the strain rate is inversely proportional to the square of the grain size. Therefore, the strain rate increases with the decrease in grain size, and the deformation also increases accordingly, thus increasing the elongation. In addition, the increase in dislocation density in the composites promotes the precipitation of the T1 phase. In the Al-Cu-Li system, the T1 phase is considered an essential strengthening phase, which can simultaneously improve the strength and ductility of the material [60,61], and the precipitation of the T1 phase will be uniform with the uniform distribution of TiB_2 particles. The composite with UT for 180 s has the best ductility due to the smallest grain size and the most uniform distribution of TiB_2 particles. Therefore, UT improves the elongation of the composites, and the elongation is the best when the UT time is 180 s. The strength and elongation of TiB_2/2195 composites prepared by ultrasonic-assisted in-situ casting have significantly improved simultaneously, and they will have certain application prospects in aerospace applications requiring light weight and high strength.

5. Conclusions

2 wt.% TiB_2/2195 composites were prepared by mixed salt reaction under the argon atmosphere using ultrasonic-assisted in-situ casting technology. Based on the results and analysis, the main conclusions are as follows:

(1) The TiB_2 particles generated in situ provided a large amount of heterogeneous nucleation for the Al matrix, which refined the grains. The average grain size was reduced from 288 μm in the remelted matrix to 159 μm, and the refinement rate was 44.8 %. At the same time, TiB_2 particles significantly increased the dislocation density in the composite and promoted the precipitation of the T1 phase. However, the TiB_2 particles were seriously agglomerated with the second phase structure.
(2) The UT further refined the grains and improved the agglomeration of the second phase structure, the TiB_2 particles became fine and dispersed, and more TiB_2 particles and Cu-containing phases were dispersed inside the grains. Compared with the composite without UT, the grain size refinement rate was 54.7 %, the reduction rate of the coarse second phase network area fraction was 32.0 %, and the mass fraction of intragranular TiB_2 particles increased by 100.0 % when ultrasonically treated for 180 s.
(3) The synergistic effect of UT and TiB_2 particles significantly improved the mechanical properties of composites. The UTS, YS, and elongation of the composite with UT for 180 s were 195.3 MPa, 86.5 MPa, and 7.62 %, respectively, which were improved by 115.4 %, 49.8 %, and 342.9 %, respectively, compared with the remelted matrix. The main contribution to the increase in YS is CTE mismatch strengthening, while the improvement in ductility may come from precipitation of the T1 phase and grain refinement.

CRediT authorship contribution statement

Ziming Xie: Methodology, Validation, Formal analysis, Investigation, Writing – original draft. **Ripeng Jiang:** Methodology, Resources, Formal analysis, Writing – review & editing. **Xiaoqian Li:** Conceptualization, Supervision, Funding acquisition. **Lihua Zhang:** Conceptualization, Project administration. **Anqing Li:** Validation, Formal analysis, Software. **Zhuoli He:** Investigation, Data curation.

Declaration of Competing Interest

The authors declare that they have no known competing financial interests or personal relationships that could have appeared to influence the work reported in this paper.

Data availability

Data will be made available on request.

Acknowledgments

This work was supported by the National Natural Science Foundation of China (Grant No. 51805549), the Project of State Key Laboratory of High Performance Complex Manufacturing at Central South University (Grant No. ZZYJKT2021.01), and the Scientific Research Fund of Hunan Provincial Education Department, China (Grant No. 20C1110).

References

[1] X. Zhang, Y. Chen, J. Hu, Recent advances in the development of aerospace materials, Prog. Aerosp. Sci. 97 (2018) 22–34, https://doi.org/10.1016/j.paerosci.2018.01.001.
[2] P. Yu, Z. Mei, S.C. Tjong, Structure, thermal and mechanical properties of in situ Al-based metal matrix composite reinforced with Al2O3 and TiC submicron particles, Mater. Chem. Phys. 93 (2005) 109–116, https://doi.org/10.1016/j.matchemphys.2005.02.028.
[3] M. Kök, Abrasive wear of Al2O3 particle reinforced 2024 aluminium alloy composites fabricated by vortex method, Compos. Part Appl. Sci. Manuf. 37 (2006) 457–464. https://doi.org/10.1016/j.compositesa.2005.05.038.
[4] M. Malaki, W. Xu, A.K. Kasar, P.L. Menezes, H. Dieringa, R.S. Varma, M. Gupta, Advanced Metal Matrix Nanocomposites, Metals. 9 (2019) 330, https://doi.org/10.3390/met9030330.
[5] G.R. Li, Y.T. Zhao, H.M. Wang, G. Chen, Q.X. Dai, X.N. Cheng, Fabrication and properties of in situ (Al3Zr+Al2O3)p/A356 composites cast by permanent mould and squeeze casting, J. Alloy. Compd. 471 (2009) 530–535, https://doi.org/10.1016/j.jallcom.2008.04.037.
[6] F. Ficici, Abrasive Wear of In Situ AlB2/Al-4Cu Composite Material Produced by Squeeze Casting Method, JOM 66 (2014) 711–719, https://doi.org/10.1007/s11837-014-0949-4.
[7] K. Tian, Y. Zhao, L. Jiao, S. Zhang, Z. Zhang, X. Wu, Effects of in situ generated ZrB2 nano-particles on microstructure and tensile properties of 2024Al matrix

composites, J. Alloy. Compd. 594 (2014) 1–6, https://doi.org/10.1016/j.jallcom.2014.01.117.
[8] M. Wang, D. Chen, Z. Chen, Y. Wu, F. Wang, N. Ma, H. Wang, Mechanical properties of in-situ TiB2/A356 composites, Mater. Sci. Eng., A 590 (2014) 246–254, https://doi.org/10.1016/j.msea.2013.10.021.
[9] S.-L. Zhang, X.-X. Shi, Y.-T. Zhao, B.-R. Zhang, Z.-P. Liang, H.-S. Yin, B.-Y. Dou, Q. Zhang, C.-X. Wang, Preparation, microstructures and mechanical properties of in-situ (TiB2 + ZrB2)/AlSi9Cu3 composites, J. Alloy. Compd. 673 (2016) 349–357, https://doi.org/10.1016/j.jallcom.2016.02.243.
[10] Y. Yang, Z. Liu, R. Jiang, R. Li, X. Li, Microstructural evolution and mechanical properties of the AA2219/TiC nanocomposite manufactured by ultrasonic solidification, J. Alloys Compd. 811 (2019) UNSP 151991. https://doi.org/10.1016/j.jallcom.2019.151991.
[11] B. Zhao, Q. Yang, L. Wu, X. Li, M. Wang, H. Wang, Effects of nanosized particles on microstructure and mechanical properties of an aged in-situ TiB2/Al-Cu-Li composite, Mater. Sci. Eng., A 742 (2019) 573–583, https://doi.org/10.1016/j.msea.2018.11.032.
[12] K. Huang, R. Jiang, X. Li, L. Zhang, Z. Li, R. Li, Effects of High-Intensity Ultrasound on Microstructure and Mechanical Property of In situ TiB2/2A14 Composites, Metals. 9 (2019) 1210, https://doi.org/10.3390/met9111210.
[13] Z. Liu, P. Xie, M. Chen, Q. Zheng, Y. Gao, Y. Liu, X. Kai, Effects of ultrasound assisted solidificaiton on the microstructure and mechanical properties of nano-sized TiB2/Al-4.5Cu composites, Materialia. 15 (2021), 101024, https://doi.org/10.1016/j.mtla.2021.101024.
[14] C. Yang, Z. Liu, Q. Zheng, Y. Cao, X. Dai, L. Sun, J. Zhao, J. Xing, Q. Han, Ultrasound assisted in-situ casting technique for synthesizing small-sized blocky Al3Ti particles reinforced A356 matrix composites with improved mechanical properties, J. Alloy. Compd. 747 (2018) 580–590, https://doi.org/10.1016/j.jallcom.2018.02.010.
[15] J. Liao, M.J. Tan, I. Sridhar, Creep behavior of spray-deposited AlLi/SiCp composite, Mater. Sci. Eng. Struct. Mater. Prop. Microstruct. Process. 527 (2010) 4906–4913, https://doi.org/10.1016/j.msea.2010.04.040.
[16] F. Dong, X. Li, L. Zhang, L. Ma, R. Li, Cavitation erosion mechanism of titanium alloy radiation rods in aluminum melt, Ultrason. Sonochem. 31 (2016) 150–156, https://doi.org/10.1016/j.ultsonch.2015.12.009.
[17] Y. Tian, Z. Liu, X. Li, L. Zhang, R. Li, R. Jiang, F. Dong, The cavitation erosion of ultrasonic sonotrode during large-scale metallic casting: Experiment and simulation, Ultrason. Sonochem. 43 (2018) 29–37, https://doi.org/10.1016/j.ultsonch.2017.12.053.
[18] Y. Zhang, R. Li, P. Chen, Y. Yang, X. Li, R. Jiang, Tuning the microstructure morphology and genetic mechanical properties of 2219 Al alloy with ultrasonic treatment, J. Alloy. Compd. 846 (2020), 156251, https://doi.org/10.1016/j.jallcom.2020.156251.
[19] G. He, C. He, Y. Liu, C. Liu, Z. Fu, S. Xu, X. Sheng, Z. Xiao, Q. Wen, Uncovering Microstructure Evolution and Dynamic Softening Mechanism of Spray-Deposited AlZnMgCu Alloy Under Thermal Deformation, Met. Mater. Int. 28 (2022) 2103–2117, https://doi.org/10.1007/s12540-021-01114-3.
[20] Y. Hu, R. Jiang, X. Li, A. Li, Z. Xie, Effects of High-Intensity Ultrasound on the Microstructure and Mechanical Properties of 2195 Aluminum Ingots, Metals. 11 (2021) 1050, https://doi.org/10.3390/met11071050.
[21] L. Zhang, X. Li, R. Li, R. Jiang, L. Zhang, Effects of high-intensity ultrasound on the microstructures and mechanical properties of ultra-large 2219 Al alloy ingot, Mater. Sci. Eng. -Struct. Mater. Prop. Microstruct. Process. 763 (2019), 138154, https://doi.org/10.1016/j.msea.2019.138154.
[22] N. Srivastava, G.P. Chaudhari, Microstructural evolution and mechanical behavior of ultrasonically synthesized Al6061-nano alumina composites, Mater. Sci. Eng., A 724 (2018) 199–207, https://doi.org/10.1016/j.msea.2018.03.092.
[23] J. Geng, G. Liu, F. Wang, T. Hong, C. Xia, M. Wang, D. Chen, N. Ma, H. Wang, Microstructural and mechanical anisotropy of extruded in-situ TiB2/2024 composite plate, Mater. Sci. Eng., A 687 (2017) 131–140, https://doi.org/10.1016/j.msea.2017.01.069.
[24] B. Huang, Y. Liu, Z. Zhou, W. Cheng, X. Liu, Selective laser melting of 7075 aluminum alloy inoculated by Al–Ti–B: Grain refinement and superior mechanical properties, Vacuum 200 (2022), 111030, https://doi.org/10.1016/j.vacuum.2022.111030.
[25] X.P. Li, G. Ji, Z. Chen, A. Addad, Y. Wu, H.W. Wang, J. Vleugels, J. Van Humbeeck, J.P. Kruth, Selective laser melting of nano-TiB2 decorated AlSi10Mg alloy with high fracture strength and ductility, Acta Mater. 129 (2017) 183–193, https://doi.org/10.1016/j.actamat.2017.02.062.
[26] D.H. StJohn, M. Qian, M.A. Easton, P. Cao, The Interdependence Theory: The relationship between grain formation and nucleant selection, Acta Mater. 59 (2011) 4907–4921, https://doi.org/10.1016/j.actamat.2011.04.035.
[27] L. Wu, C. Zhou, X. Li, N. Ma, H. Wang, Microstructural evolution and mechanical properties of cast high-Li-content TiB2/Al-Li-Cu composite during heat treatment, J. Alloy. Compd. 739 (2018) 270–279, https://doi.org/10.1016/j.jallcom.2017.12.126.
[28] H. Li, P. Chen, Z. Wang, F. Zhu, R. Song, Z. Zheng, Tensile properties, microstructures and fracture behaviors of an Al-Zn-Mg-Cu alloy during ageing after solution treating and cold-rolling, Mater. Sci. Eng., A 742 (2019) 798–812, https://doi.org/10.1016/j.msea.2018.03.098.
[29] T. Mo, Z. Chen, Z. Zhou, J. Liu, W. He, Q. Liu, Enhancing of mechanical properties of rolled 1100/7075 Al alloys laminated metal composite by thermomechanical treatments, Mater. Sci. Eng., A 800 (2021), 140313, https://doi.org/10.1016/j.msea.2020.140313.
[30] S. Jayalakshmi, S. Gupta, S. Sankaranarayanan, S. Sahu, M. Gupta, Structural and mechanical properties of Ni60Nb40 amorphous alloy particle reinforced Al-based composites produced by microwave-assisted rapid sintering, Mater. Sci. Eng., A 581 (2013) 119–127, https://doi.org/10.1016/j.msea.2013.05.072.
[31] B.I. Rodgers, P.B. Prangnell, Quantification of the influence of increased pre-stretching on microstructure-strength relationships in the Al–Cu–Li alloy AA2195, Acta Mater. 108 (2016) 55–67, https://doi.org/10.1016/j.actamat.2016.02.017.
[32] B.M. Gable, A.W. Zhu, A.A. Csontos, E.A. Starke, The role of plastic deformation on the competitive microstructural evolution and mechanical properties of a novel Al–Li–Cu–X alloy, J. Light Met. 1 (1) (2001) 1–14.
[33] G.I. Eskin, D.G. Eskin, Ultrasonic Treatment of Light Alloy Melts, 2nd ed., CRC Press, Boca Raton, 2014. https://doi.org/10.1201/b17270.
[34] A. Priyadarshi, M. Khavari, S. Bin Shahrani, T. Subroto, L.A. Yusuf, M. Conte, P. Prentice, K. Pericleous, D. Eskin, I. Tzanakis, In-situ observations and acoustic measurements upon fragmentation of free-floating intermetallics under ultrasonic cavitation in water, Ultrason. Sonochem. 80 (2021), 105820, https://doi.org/10.1016/j.ultsonch.2021.105820.
[35] D.G. Eskin, I. Tzanakis, F. Wang, G.S.B. Lebon, T. Subroto, K. Pericleous, J. Mi, Fundamental studies of ultrasonic melt processing, Ultrason. Sonochem. 52 (2019) 455–467, https://doi.org/10.1016/j.ultsonch.2018.12.028.
[36] I. Tzanakis, G.S.B. Lebon, D.G. Eskin, K.A. Pericleous, Characterizing the cavitation development and acoustic spectrum in various liquids, Ultrason. Sonochem. 34 (2017) 651–662, https://doi.org/10.1016/j.ultsonch.2016.06.034.
[37] Y. Zhang, R. Li, X. Li, Y. Yang, P. Chen, F. Dong, R. Jiang, Possible Effects and Mechanisms of Ultrasonic Cavitation on Oxide Inclusions during Direct-Chill Casting of an Al Alloy, Metals. 8 (2018) 814, https://doi.org/10.3390/met8100814.
[38] G.I. Eskin, Improvement of the Structure and Properties of Ingots and Worked Aluminum Alloy Semifinished Products by Melt Ultrasonic Treatment in a Cavitation Regime, Metallurgist. 54 (2010) 505–513, https://doi.org/10.1007/s11015-010-9331-0.
[39] G.I. Eskin, D.G. Eskin, Production of natural and synthesized aluminum-based composite materials with the aid of ultrasonic (cavitation) treatment of the melt, Ultrason. Sonochem. 10 (2003) 297–301, https://doi.org/10.1016/S1350-4177(02)00158-X.
[40] Y. Zhang, R. Li, P. Chen, X. Li, Z. Liu, Microstructural evolution of Al2Cu phase and mechanical properties of the large-scale Al alloy components under different consecutive manufacturing processes, J. Alloy. Compd. 808 (2019) 151634.
[41] Z.Y. Xu, C.F. Fang, R. Wang, C.Y. Zhong, Y.M. Wang, Microstructural evolution, strengthening and toughening mechanisms of AZ80 composite sheet reinforced by TiB2 with fiber-like distribution, J. Alloy. Compd. 877 (2021), 160278, https://doi.org/10.1016/j.jallcom.2021.160278.
[42] S.A. Sajjadi, H.R. Ezatpour, M. Torabi Parizi, Comparison of microstructure and mechanical properties of A356 aluminum alloy/Al2O3 composites fabricated by stir and compo-casting processes, Mater. Des. 34 (2012) 106–111, https://doi.org/10.1016/j.matdes.2011.07.037.
[43] C.D. Li, X.J. Wang, W.Q. Liu, K. Wu, H.L. Shi, C. Ding, X.S. Hu, M.Y. Zheng, Microstructure and strengthening mechanism of carbon nanotubes reinforced magnesium matrix composite, Mater. Sci. Eng., A 597 (2014) 264–269, https://doi.org/10.1016/j.msea.2014.01.008.
[44] M.J. Starink, P. Wang, I. Sinclair, P.J. Gregson, Microstrucure and strengthening of Al–Li–Cu–Mg alloys and MMCs: II, Modelling of yield strength, Acta Mater. 47 (1999) 3855–3868, https://doi.org/10.1016/S1359-6454(99)00228-1.
[45] A. Fadavi Boostani, S. Yazdani, R. Taherzadeh Mousavian, S. Tahamtan, R. Azari Khosroshahi, D. Wei, D. Brabazon, J.Z. Xu, X.M. Zhang, Z.Y. Jiang, Strengthening mechanisms of graphene sheets in aluminium matrix nanocomposites, Mater. Des. 88 (2015) 983–989, https://doi.org/10.1016/j.matdes.2015.09.063.
[46] N. Srivastava, G.P. Chaudhari, Strengthening in Al alloy nano composites fabricated by ultrasound assisted solidification technique, Mater. Sci. Eng., A 651 (2016) 241–247, https://doi.org/10.1016/j.msea.2015.10.118.
[47] Z. Zhang, D.L. Chen, Contribution of Orowan strengthening effect in particulate-reinforced metal matrix nanocomposites, Mater. Sci. Eng., A 483–484 (2008) 148–152, https://doi.org/10.1016/j.msea.2006.10.184.
[48] L.H. Dai, Z. Ling, Y.L. Bai, Size-dependent inelastic behavior of particle-reinforced metal–matrix composites, Compos. Sci. Technol. 61 (2001) 1057–1063, https://doi.org/10.1016/S0266-3538(00)00235-9.
[49] B.P. Sahoo, D. Das, A.K. Chaubey, Strengthening mechanisms and modelling of mechanical properties of submicron-TiB2 particulate reinforced Al 7075 metal matrix composites, Mater. Sci. Eng., A 825 (2021), 141873, https://doi.org/10.1016/j.msea.2021.141873.
[50] T. Wang, Z. Chen, Y. Zheng, Y. Zhao, H. Kang, L. Gao, Development of TiB2 reinforced aluminum foundry alloy based in situ composites – Part II: Enhancing the practical aluminum foundry alloys using the improved Al–5wt%TiB2 master composite upon dilution, Mater. Sci. Eng., A 605 (2014) 22–32, https://doi.org/10.1016/j.msea.2014.03.021.
[51] J. Liu, Z. Liu, Z. Dong, X. Cheng, Q. Zheng, J. Li, S. Zuo, Z. Huang, Y. Gao, J. Xing, Q. Han, On the preparation and mechanical properties of in situ small-sized TiB2/Al-4.5Cu composites via ultrasound assisted RD method, J. Alloy. Compd. 765 (2018) 1008–1017, https://doi.org/10.1016/j.jallcom.2018.06.303.
[52] Z. Zhang, D.L. Chen, Consideration of Orowan strengthening effect in particulate-reinforced metal matrix nanocomposites: A model for predicting their yield strength, Scr. Mater. 54 (2006) 1321–1326, https://doi.org/10.1016/j.scriptamat.2005.12.017.
[53] J. Xiang, L. Xie, S.A. Meguid, S. Pang, J. Yi, Y. Zhang, R. Liang, An atomic-level understanding of the strengthening mechanism of aluminum matrix composites reinforced by aligned carbon nanotubes, Comput. Mater. Sci. 128 (2017) 359–372, https://doi.org/10.1016/j.commatsci.2016.11.032.

[54] Z. Zhang, T. Topping, Y. Li, R. Vogt, Y. Zhou, C. Haines, J. Paras, D. Kapoor, J. M. Schoenung, E.J. Lavernia, Mechanical behavior of ultrafine-grained Al composites reinforced with B4C nanoparticles, Scr. Mater. 65 (2011) 652–655, https://doi.org/10.1016/j.scriptamat.2011.06.037.

[55] C.-S. Kim, I. Sohn, M. Nezafati, J.B. Ferguson, B.F. Schultz, Z. Bajestani-Gohari, P. K. Rohatgi, K. Cho, Prediction models for the yield strength of particle-reinforced unimodal pure magnesium (Mg) metal matrix nanocomposites (MMNCs), J. Mater. Sci. 48 (2013) 4191–4204, https://doi.org/10.1007/s10853-013-7232-x.

[56] Y. Hu, R. Jiang, X. Li, R. Hu, Effect of Ultrasonic-Assisted Casting on the Hydrogen and Lithium Content of Al-Li Alloy, Materials. 15 (2022) 1081, https://doi.org/10.3390/ma15031081.

[57] X. Liu, Z. Zhang, W. Hu, Q. Le, L. Bao, J. Cui, J. Jiang, Study on hydrogen removal of AZ91 alloys using ultrasonic argon degassing process, Ultrason. Sonochem. 26 (2015) 73–80, https://doi.org/10.1016/j.ultsonch.2014.12.015.

[58] H. Xu, X. Jian, T.T. Meek, Q. Han, Degassing of molten aluminum A356 alloy using ultrasonic vibration, Mater. Lett. 58 (2004) 3669–3673, https://doi.org/10.1016/j.matlet.2004.02.055.

[59] D.G. Eskin, I. Tzanakis, High-Frequency Vibration and Ultrasonic Processing, in: D. G. Eskin, J. Mi (Eds.), Solidif. Process. Met. Alloys Extern. Fields, Springer International Publishing, Cham, 2018: pp. 153–193. https://doi.org/10.1007/978-3-319-94842-3_5.

[60] S. Zhang, W. Zeng, W. Yang, C. Shi, H. Wang, Ageing response of a Al–Cu–Li 2198 alloy, Mater. Des. 63 (2014) 368–374, https://doi.org/10.1016/j.matdes.2014.04.063.

[61] A. Medjahed, A. Henniche, M. Derradji, T. Yu, Y. Wang, R. Wu, L. Hou, J. Zhang, X. Li, M. Zhang, Effects of Cu/Mg ratio on the microstructure, mechanical and corrosion properties of Al-Li-Cu-Mg-X alloys, Mater. Sci. Eng., A 718 (2018) 241–249, https://doi.org/10.1016/j.msea.2018.01.118.